Ultra-Wideband Channel Model for Communication Around the Human Body

Andrew Fort, *Student Member, IEEE*, Julien Ryckaert, Claude Desset, *Member, IEEE*, Philippe De Doncker, Piet Wambacq, *Member, IEEE*, and Leo Van Biesen, *Member, IEEE*

***Abstract*—Using ultra-wideband (UWB) wireless sensors placed on a person to continuously monitor health information is a promising new application. However, there are currently no detailed models describing the UWB radio channel around the human body making it difficult to design a suitable communication system. To address this problem, we have measured radio propagation around the body in a typical indoor environment and incorporated these results into a simple model. We then implemented this model on a computer and compared experimental data with the simulation results. This paper proposes a simple statistical channel model and a practical implementation useful for evaluating UWB body area communication systems.**

***Index Terms*—Body area network, channel model, ultra-wideband (UWB).**

I. Introduction

USING wireless sensors around the body to monitor health information is a promising new application made possible by recent advances in ultra low power technology. Each sensor continuously measures parameters of interest and sends the data to a central device such as a personal digital assistant (PDA). Examples include sensors to observe brain activity for recording or warning against seizures, or sensors to examine heart activity for diagnosis and automatic emergency calls.

Ultra-wideband (UWB) has recently received attention as a promising air interface for short-range low-data-rate communication matching the requirements of wireless bio-medical applications. Furthermore, the Federal Communications Commission (FCC) has recently legalized a spectral mask between 3.1–10.6 GHz for UWB. Finally, the IEEE 802.15.4a committee is developing a low-power UWB standard and included body area networks (BANs) as a relevant scenario [1].

Unfortunately, there are no UWB BAN channel models required for wireless bio-medical system design. Past attempts focused on finite-difference time-domain (FDTD) simulations [2]. However, the computational complexity of the FDTD method limited simulations to scenarios that did not include an indoor environment or small antennas. UWB measurements have also been reported [3]–[5]. However, these studies do not propose a complete model.

Manuscript received March 1, 2005; revised October 20, 2005. This work was supported by the MEDEA+ Witness Project.

A. Fort and P. Wambacq are with the IMEC, Kapeldreef 75, B3001 Leuven, Belgium, and also with the Vrije Universiteit Brussel, B-1050 Brussel, Belgium (e-mail: forta@imec.be).

J. Ryckaert and C. Desset are with IMEC, B3001 Leuven, Belgium.

P. De Doncker is with the Universite Libre de Bruxelles, Ondes et Signaux, B1050 Bruxelles, Belgium.

L. Van Biesen is with the Vrije Universiteit Brussel, B-1050 Brussel, Belgium.

Digital Object Identifier 10.1109/JSAC.2005.863885

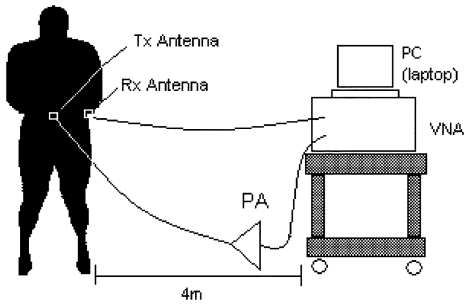

Fig. 1. Experiment setup.

To address problems with BAN channel characterization, we have used a vector network analyzer (VNA) and small antennas to obtain several channel responses around a human torso in an office. Based on the extracted responses, we estimate channel statistics and incorporate them into a model. Finally, we implement this model and compare it with the measurements. We focus on the 3–6-GHz band which is commonly proposed for UWB systems.

This paper describes our propagation study. Sections II and III present the experiment and analysis of propagation near the body. Sections IV and V describe the experiment and analysis extending these results to include an office room. Section VI combines the model near the body with that of an indoor environment in an implementation of the complete radio channel. Finally, Section VII summarizes all results.

II. Experiment Setup: Propagation Near a Body

Fig. 1 shows the setup for measurements near the body. In all cases, the body is in a standing position with arms hanging along the side. An HP8753SE VNA measures the S21 parameter between two antennas on a body. The two antennas are connected to the VNA using low-loss coaxial cables. An Agilent 87 415A amplifier[1] helps to increase the dynamic range. All measurements in this section are made in a large empty room so that propagation near the body can be separated from later reflections.

The same small-size, low-profile Skycross SMT-3TO10M UWB antennas[2] are used for all measurements. The antennas are mounted on the torso, as shown in Fig. 2, so that they are linearly polarized parallel with the body. We control the separation by placing either a 5- or 10-mm dielectric between the body and the antenna. The antenna size and separation reflect the dimensions of current body worn system in a package prototypes [6].

[1]Agilent Technologies, Palo Alto, CA (http://www.home.agilent.com)

[2]Skycross, Viera, FL (http://www.skycross.com)

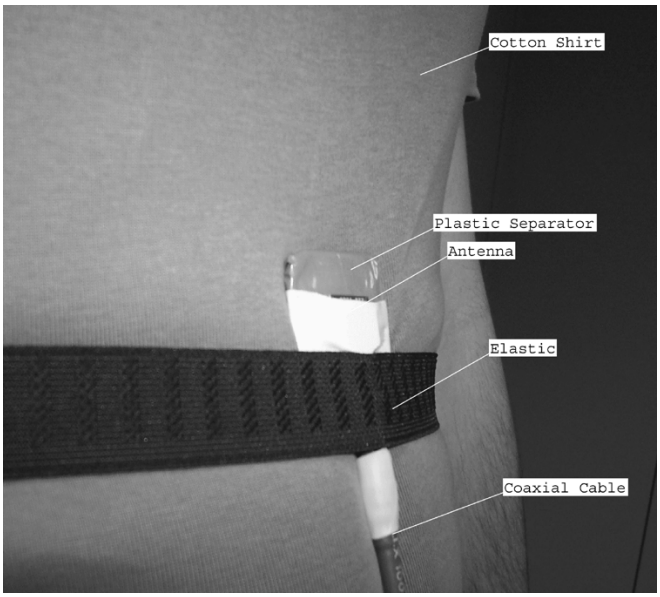

Fig. 2. Antenna mounted on body.

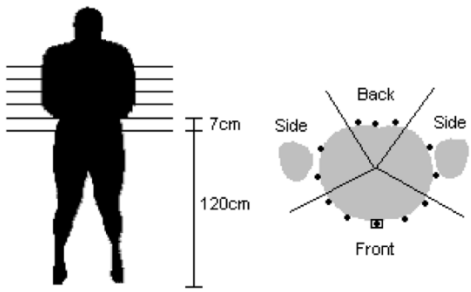

Fig. 3. Measurement locations on body.

We analyze the antenna matching by measuring the S11 parameter in free space and close to the body. In free space, the S11 parameter is below -10 dB across the band of interest indicating the measurement setup itself does not introduce significant loss. The matching is also good for a separation of 5 mm and 10 mm, but becomes marginal when the antenna is placed almost directly on the body ($S11 < -5$ dB). This will be discussed further in our analysis.

Due to the small-size UWB antennas used in these measurements, the coaxial cable and connector may influence antenna parameters. However, the display on our VNA remains stable when we move the cables indicating they do not radiate enough energy to appreciably alter our results. An alternative approach using a fiber-optic link was proposed in [5]. Unfortunately, this requires a nearby optic receiver and battery which also influences radiation characteristics. Moreover, integrating small antennas into electronic sensors will invariably alter their radiation characteristics. We, therefore, see no advantage in using special cables or connectors.

Fig. 3 shows where the antennas are placed on the body. All parameters are extracted from measurements performed in six planes separated by 7 cm along the z axis of the torso (see left diagram). The right diagram shows where the antennas are placed on the body for each plane. The receiver positions are marked with circles, while the transmitter position is marked with a box around the circle. The transmitter is always placed on the front of the body, and the receiver is placed at various positions on the torso at distances of 10–45 cm. We record measurements one plane above and one plane below the transmitter at each distance to obtain 144 measurements at various receiver positions.

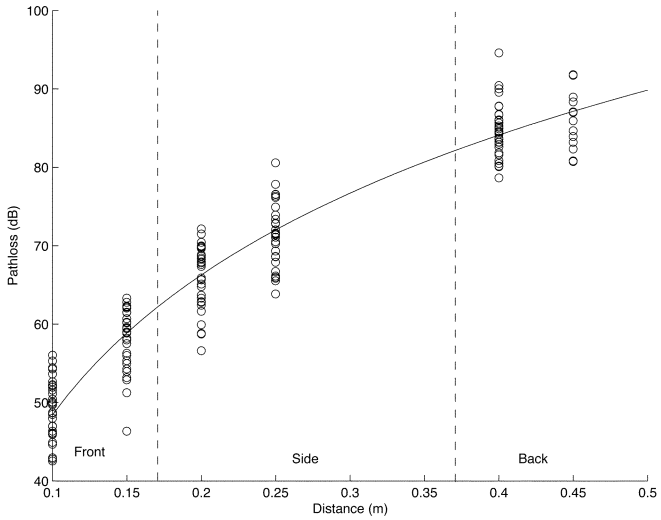

Fig. 4. Measured path loss around the body (5-mm separation).

Channel parameters may depend on the position of the antenna around the body [2], [3], [5], [7]. We, therefore, extract parameters separately in regions representing the front, side, and back of the body (see right diagram).

III. Analysis of Propagation Near the Body

For communication between sensors placed on the body, transmitted signals can arrive at the receiver in three ways:

1) propagation through the body;
2) diffraction around the body;
3) reflections off of nearby scatterers then back at the body.

Propagation through the body is negligible in the gigahertz frequency range and can be ignored [2]. We propose measuring and modeling the local components diffracting around the body separately from the components reflecting from the surrounding environment for several reasons. The local diffracting components have different properties from the reflected components requiring different modeling and measurement procedures. Furthermore, this approach allows the reuse of existing propagation measurements near the body for any indoor environment.

The measured frequency domain transfer-function is converted to the time domain using an inverse Fourier transform. With no special windowing of the data, we observe significant sidelobes in the time domain. A window function can be applied to reduce these sidelobes at the cost of a decrease in the measurement resolution. Initial experimentation indicated that a Hamming window provides a better compromise.

Since the body is within the near field of the antenna, charges on both the antenna and body surfaces interact to create a single radiating system. In this case, it is no longer possible to separate the influence of the antenna from the influence of the body. We, therefore, include the antenna as a part of the channel model throughout this analysis.

A. Path Loss

Fig. 4 shows the path loss versus distance trend. The vertical axis represents the measured path loss. The horizontal axis is the distance traveled by the wave around the perimeter of the body.

TABLE I
PATH LOSS PARAMETERS FOR DIFFERENT ANTENNA–BODY SEPARATIONS

Parameter	*0 mm*	*5 mm*	*10 mm*
n	5.8	5.9	6.0
d_0 (m)	0.1	0.1	0.1
P_{0dB}	56.1	48.4	45.8

The average path loss is usually modeled with the following power decay law:

$$P_{\mathrm{dB}} = P_{0\ \mathrm{dB}} + 10n \log\left(\frac{d}{d_0}\right). \tag{1}$$

The parameters of this path model extracted from the measurements are shown in Table I. The excellent fit of this model to the data is shown in Fig. 4. Compared with free space $(n = 2)$, the path loss exponent near the body in the gigahertz range is much higher $(n = 6)$. This exponent is consistent with previous gigahertz range studies around the human torso where n is estimated between 5 and 7.4 [2], [4], [8]. However, lower exponents $(n = 3)$ are reported when propagation is along the front rather than around the torso [3], [4].

Table I demonstrates that the path loss exponent does not depend significantly on the antenna–body separation because after the wave is radiated beyond the near field, it propagates independently from the source. However, the reference path loss (P_0) associated with losses near the antenna increases as the antenna is closer to the body. Several effects contribute to this including mismatch loss, higher energy absorption by the human tissue, and changes in the radiation pattern.

Several UWB studies have proposed a frequency-dependent path loss model [9]. The peak gain of our Skycross antennas varies by only 1.5 dB between 3–6 GHz[2]. Nevertheless, we observe both positive and negative slopes in addition to dips in the frequency response consistent with [5]. This can be attributed to the antenna radiating properties changing at different locations on the body. Since we do not observe significant frequency dependency when the responses are averaged over all the measurements, we use a frequency-independent *average* path loss law. Frequency dependency of individual measurements will introduce correlations in the time-domain amplitude distributions, as discussed in Section III-C.

The path loss law may need to be modified for frequency-dependent antennas. Furthermore, the law will not hold at lower frequencies where we expect signal penetration through the body. In this case, the loss depends on the skin depth of body tissues resulting in frequency dependence [10].

B. Power Delay Profile

A convenient characterization of propagation channels is the discrete-time impulse response model [11], [12]. In this model, the time axis is quantized into "bins." The first bin corresponding to the first multipath component (MPC) is determined manually. Each bin is assigned an amplitude corresponding to the energy integrated in that bin. The bin width depends on the measurement resolution which is approximated as the reciprocal of the bandwidth swept (0.33 ns) multiplied by the additional window function bandwidth. The 6-dB bandwidth of the Hamming window is 1.5 times wider than the rectangular window resulting in a 0.5-ns resolution.

By averaging the energy in each bin over all measurements, we obtain the average power delay profile. The energy decays approximately exponentially. The decay rates depend on the position of the receiver: -13.4 dB/ns on the front, -10.7 dB/ns on the side, and -7.8 dB/ns on the back. The longer impulse response on the back and side of the body compared with the front is consistent with trends reported in [2]–[4], [7]. This effect is probably due to multiple paths reflecting or diffracting around the body.

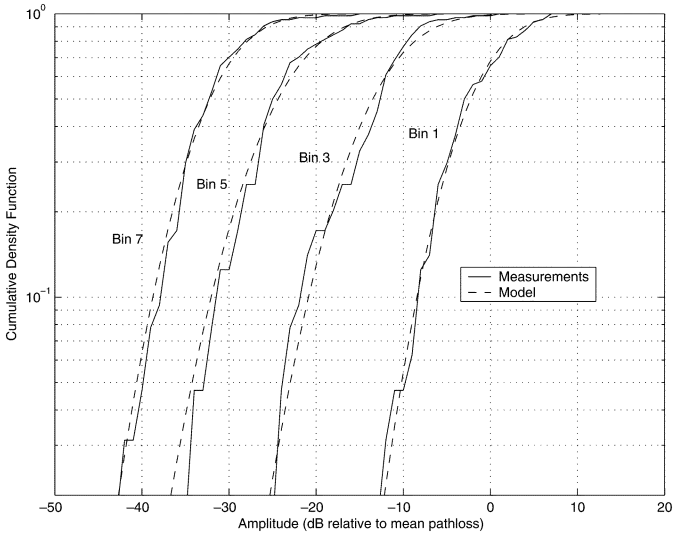

Fig. 5. Amplitude cumulative density functions (side of body).

C. Amplitude Distribution

In UWB systems, each resolved component is due to a small number of scatterers and the amplitude distribution in each bin can be different [11]. Therefore, we extract the amplitude distribution of every bin individually.

To determine the amplitude distribution, the mean path loss law is removed. The Nakagami-*m*, Rayleigh, and Lognormal distributions are then fit to the data. Analysis of the Akaike Information Theoretic Criterion [13] indicates that the Lognormal distribution is the superior model. The other distributions have only a negligible probability of being the best model.

Several empirical and theoretical Lognormal distributions obtained along the side of the body are reproduced in Fig. 5. Visual inspection show an excellent Lognormal fit to the data. Slightly higher variances are observed on the side of the body $(\sigma \approx 5$–6 dB) compared with on the front and back of the body $(\sigma \approx 4$–5 dB) and may be due to nearby reflections off of the arms and shoulders.

Log amplitude correlation coefficients as high as 0.8 are estimated between adjacent bins and decrease with increasing bin separation. Frequency-dependent slopes of individual measurements can spread the same pulse over multiple bins contributing to this correlation. Several other effects can also contribute including wavelength dispersion, short path lengths, and overlapping path trajectories near the antennas.

IV. INDOOR ENVIRONMENT EXPERIMENT SETUP

Measurements inside an indoor office are made with the same setup, as in Section II. Only MPCs due to reflections off of the indoor environment arriving after the diffracting waves are considered in this section.

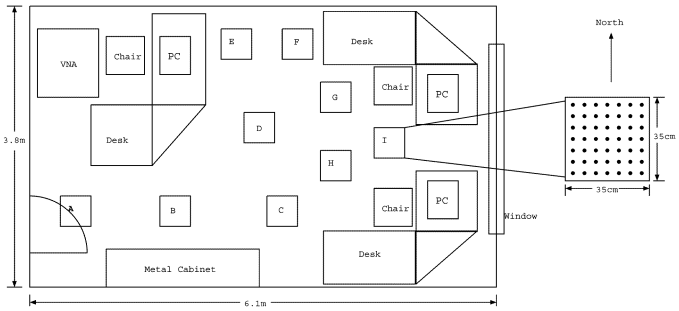

Fig. 6. Floor plan.

Fig. 6 shows a scale floor plan of the 3.7 × 6.1 × 2.8-m office room used to extract channel parameters. 100-ns-long multipath profiles are measured at nine locations around the office labeled alphanumerically. At each of the nine locations in the room, impulse responses are measured at 49 points arranged in a fixed-height 7 × 7 square grid. The separation between the array elements is set to 5 cm corresponding to half the wavelength at the lowest frequency of interest (3.1 GHz). This allows independent fading at all measured frequencies in an area small enough that large-scale parameters are identical.

The experimental procedure involves taking measurements between antennas worn on a person at marked locations in the room. The person is facing the east wall. The transmitter is placed on the front of the body, and the receiver is placed on either the front (10 cm distance), the side (20 cm distance), or the back of the body (45 cm distance). In all cases, the antenna is separated from the body by 5 mm.

A paper mat is placed at each of the nine measurement locations in the room. Each map contains a grid of points telling the person where to stand to make the 49 different measurements at one location. A laptop is programmed to take measurements and then signal the person to move to the next measurement point.

V. Analysis of a Body in an Indoor Environment

We process all the profiles measured in the nine locations and obtain 9×49 power delay profiles (PDPs) for each of the receiver positions (front, side, and back). We separately analyze the *large-* and *small*-scale statistics. In our analysis, large-scale statistics refer to variations when a person moves to different locations in the same room. Small-scale statistics refer variations due to a very small change in the user position while the environment near the user does not change significantly.

We refer to the PDP measured at one of the 9×49 locations as the *local* PDP, while the PDP averaged over the 49 locations is the *averaged* PDP (APDP). This spatial averaging mostly removes the small-scale fading. The delay axis of the PDPs is quantized into 0.5-ns bins.

A. Path Gain and Large-Scale Fading of Reflected Components

We manually locate the first cluster of reflected components arriving after the cluster diffracting around the body. By integrating the APDP over all subsequent delay bins, we obtain the total average energy received due to MPCs reflecting off of the surrounding environment and arriving back at the body which we denote $\overline{G_{\rm tot}}$.

A common model used to describe variation in large-scale path gain is the Lognormal distribution [11], [12]. Table II shows the estimated mean and standard deviation of the received energy along the front, side, and back. Note that the gain values in Table II do not include the energy of the diffracting component which we model separately in Section III. Clearly, more energy is reflected from the surrounding environment when the antennas are on the same side of the body compared with when they are on different sides of the body. Signal components arriving at the receiver on a different side of the body may take longer and more indirect paths. Thus, the received reflected energy is lower on average and has a larger variance.

TABLE II
Received Energy Reflected From the Indoor Environment

Position	$\overline{G_{tot}}, \mu_{dB}$	$\overline{G_{tot}}, \sigma_{dB}$
Front	-69.1	0.9
Side	-72.6	3.1
Back	-77.5	2.5

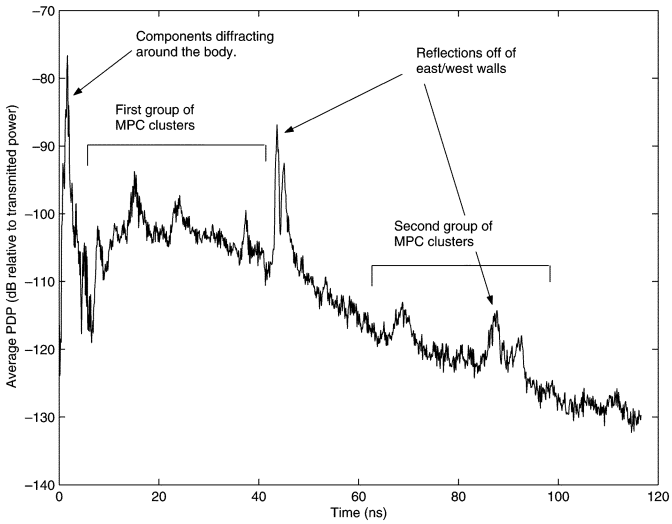

Fig. 7. Average PDP. Receiver on the side of the body.

Comparing Table II with Fig. 4 shows that if the antennas are on the same side of the body, the received energy due to MPCs reflecting off of nearby scatterers is significantly smaller than the energy of components near the body and can be ignored. However, if antennas are on different sides of the body, the reflected components become important as the initial diffracting wave is significantly attenuated.

B. Power Delay Profile

The power delay profile of reflected components has a complicated shape consisting of several random overlapping clusters as well as more deterministic clusters due to the particular geometry of our office and the orientation of the body during the measurements. We can model the random components using a modified Saleh–Valenzuela (SV) model to describe the cluster decay rates (Section V-B-1) and arrival times (Section V-B-2). We treat the deterministic clusters separately (Section V-B-3).

1) Cluster and Ray Decay Rates: Fig. 7 shows the APDP taken at one location when the receiver is worn on the side of the body. First, a cluster of MPCs is observed shortly after transmission. This is due to diffraction around the body and was analyzed in Section III. Second, a group of overlapping MPC clusters is observed due to reflections off nearby scatterers in the room. Finally, a second group of clusters arrives some time later. The

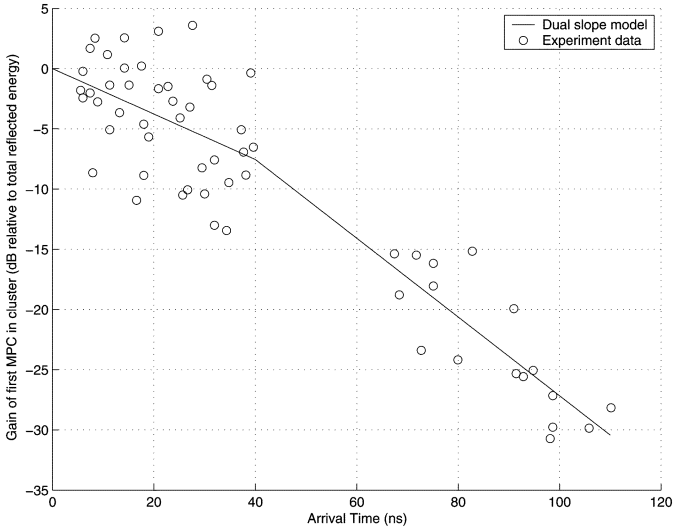

Fig. 8. Observed clusters. Receiver worn on the side of the body.

arrival time of the second group of clusters suggests that it is due to a main wave reflecting off both east and west walls and then again off of obstacles near the body.

We characterize these clusters by manually identifying the arrival time and magnitude of individual clusters from each APDP. The clusters are complex consisting of a wide variety of effects depending on the specific objects causing the scattering. As a simplification, we assume that all clear local maxima in the APDP correspond to a separate cluster.

Fig. 8 shows the clusters extracted from all measurements taken when the receiver is worn on the side of the body. The horizontal axis shows the time of arrival of each cluster, while the vertical axis shows the magnitude of the first bin in each cluster corresponding to the cluster peak.

Traditionally, clusters are assumed to decay exponentially with arrival time [14]. However, we found that the second group of clusters decays more rapidly than the first group and that there is a significant variance around the average trend. Therefore, the following dual slope model is more appropriate:

$$\overline{G_{\rm dB}}(\tau_l) = \begin{cases} \Gamma_1 \tau_l + G_\sigma n, & \tau_l \le \tau_{bp} \\ \Gamma_1 \tau_{bp} + \Gamma_2(\tau_l - \tau_{bp}) + G_\sigma n, & \tau_l > \tau_{bp}. \end{cases} \quad (2)$$

$\overline{G_{\rm dB}}(\tau_l)$ represents the magnitude of the cluster arriving at excess delay τ_l expressed in decibels. Γ_l and Γ_2 are the cluster decay rates of the first and second group while G_σ is the standard deviation around the average trend. n is a unit mean unit variance normally distributed random variable. The cluster decay rates and variance of this model extracted from our measurements are given in Table III, while the distribution of the cluster arrival times (τ_l) is discussed in Section V-B-2. We have chosen a break point of $\tau_{bp} = 40$ ns corresponding to a path length twice the distance between the east and west walls. We simplify our model by ignoring clusters arriving after the breakpoint since they are very small.

Small antennas become highly directional when placed on the body regardless of their radiation pattern in free space [3], [5]. Therefore, the magnitude of clusters depends both on their arrival time and their direction of arrival resulting in the large variance around the mean decay rate. The large variance combined with the small decay rates and closely spaced clusters

TABLE III
CLUSTER AND RAY DECAY MODEL PARAMETERS

Receiver Position	Γ_1 (dB/ns)	t_{bp} (ns)	Γ_2 (dB/ns)	G_σ (dB)	γ (dB/ns)
Front	-0.15	40	-0.52	3.3	2.4
Side	-0.19	40	-0.33	4.1	1.5
Back	-0.11	-	-	2.7	1.3

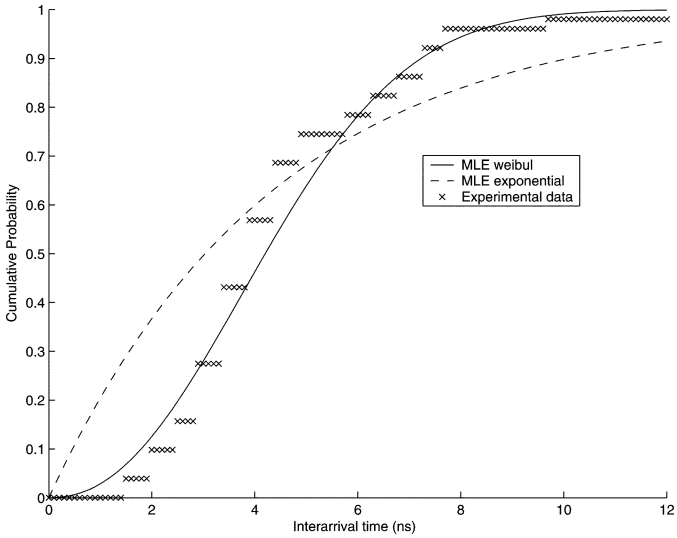

Fig. 9. Cluster interarrival times (receiver on the side of the body).

can cause later arriving clusters to be larger than earlier clusters, as shown in Fig. 7. Thus, while Fig. 8 provides an average trend across all our measurements, individual PDPs can appear to decay unevenly.

Multipath components within a cluster decay approximately exponentially with slope γ

$$\overline{G_{\rm dB}}(\tau_l + \tau_k) = \overline{G_{\rm dB}}(\tau_l) + \gamma \tau_k. \quad (3)$$

Average values of γ extracted from measurements are given in Table III. This is a simplification since γ varies for different clusters and some clusters have more complex shapes.

2) Arrival Time Statistics: Fig. 9 shows the cumulative density function (CDF) for interarrival times of clusters in the first cluster group when the receiver is on the side of the body. The exponential distribution is often associated with cluster inter-arrival times [14] but it is clear from the dashed line in Fig. 9 that it provides a poor fit to our data. This is likely due to nonrandomness of the local structure or difficulty resolving very closely spaced clusters [12]. Both of these phenomenon are likely to occur for measurements in a single room.

The Weibull distribution provides a better fit to the data (see the solid line in Fig. 9). The Weibull probability density function can be used to determine the cluster arrival times, τ_l, from (4). The maximum-likelihood (ML) estimates of the α and β parameters on each side of the body are given in Table IV.

$$p(\tau_l|\tau_{l-1}) = \frac{\alpha}{\beta^\alpha}(\tau_l - \tau_{l-1})^{\alpha-1} e^{-(\tau_l - \tau_{l-1}/\beta)^\alpha}, \quad \tau_{l-1} < \tau_l < \infty. \quad (4)$$

Our office provides a rich scattering environment so that we are unable to resolve individual MPCs. We, therefore, recommend setting the inter-arrival time of MPCs within a cluster to the effective resolution of our setup (0.5 ns).

TABLE IV
CLUSTER ARRIVAL TIME PARAMETERS (IN ns)

Position	α	β
Front	0.03	2.21
Side	0.01	2.11
Back	0.02	2.33

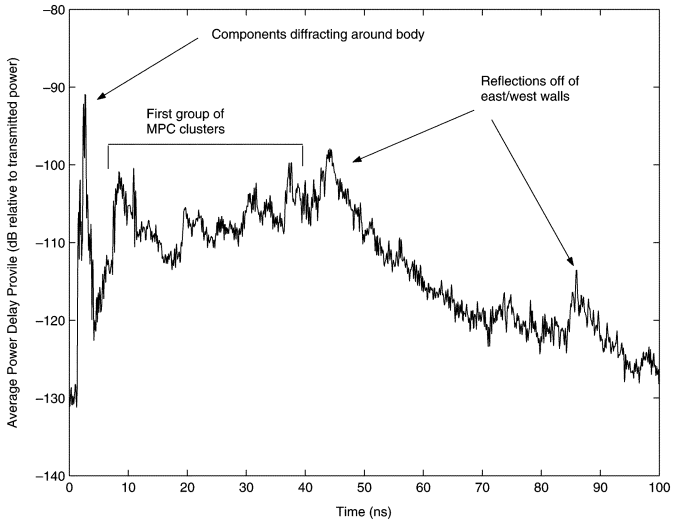

Fig. 10. Average PDP. Receiver worn on the back of the body.

3) Deterministic Components: Fig. 10 shows the APDP at position I when the receiver is on the back of the body. As before, there is a first group of clusters due to reflections off nearby scatterers. However, rather than a second group of clusters, we observe two large clusters arriving at 42 and 84 ns regardless of where the body is in the room. We see the same clusters on the side of the body, as indicated in Fig. 7.

We determined that the two clusters marked in Figs. 7 and 10 are due to the first and second reflections off the east and west walls. They always arrive at the same time since body-worn transmitters and receivers move together through the room. They are specific to our room geometry and the orientation of the body during the measurements. We, therefore, model these deterministic components separately. Rather than using the Weibull distribution, we set the arrival time of these clusters to 42 and 84 ns corresponding to twice and four times the length of our room. Rather than the exponential decay model from Table III, the gain is approximately Lognormal with parameters summarized in Table V.

Table V demonstrates that the deterministic clusters are larger with the receiver worn on the back compared with the side. This is because the radiation pattern of antennas worn on the body is directed away from the torso, since the body absorbs energy directed toward it [3]. The clusters are, therefore, smaller on the side of the body since the antenna is directed toward the south while the components are arriving from the west. The clusters are never observed when the receiver is on the front since they are shadowed by the body.

C. Small-Scale Fading

We characterize the small-scale statistics by fitting the received energies in each bin at the 49 locations of the measurement grids to Rayleigh, Lognormal, and Nakagami-*m* distributions. The Akaike Criterion indicates that the Lognormal distribution is the best model in 51% of all the bins, while the Nakagami-*m* distribution is the best model in 49% of the bins. In most cases, the Rayleigh distribution has only a negligible probability of being the best model. This is likely because there are not enough MPCs falling into a resolvable bin to justify the central limit. These results have been confirmed graphically for several bins. The mean and standard deviation for the parameters are given in Table VI. While the small-scale distribution can be different in each bin contributing to the variances in Table VI, we do not detect significant trends in the parameters for different body positions or excess delays.

TABLE V
LOGNORMAL PARAMETERS OF THE DETERMINISTIC CLUSTER GAIN

Receiver position	*First Cluster*		*Second Cluster*	
	μ_{dB}	σ_{dB}	μ_{dB}	σ_{dB}
Side	-3.7	4.4	-15.0	4.0
Back	4.8	3.8	-9.2	6.9

TABLE VI
EXTRACTED PARAMETERS FOR SMALL SCALE FADING DISTRIBUTION

	Nakagami	*Lognormal*	
	m	μ_{dB}	σ_{dB}
Average Value	1.5	-1.7	4.1
Standard deviation	0.5	0.7	0.7

The average correlation coefficient of the small-scale fading between adjacent bins over all measurements is 0.35 and becomes negligible in nonadjacent bins. This correlation may result from the same MPCs being categorized into different bins across the measurement grid. We have simplified our model by assuming each bin fades independently.

VI. CHANNEL MODEL IMPLEMENTATION

We have implemented the complete body area propagation model in Matlab. The first portion of the impulse response due to waves diffracting around the body is generated using correlated Lognormal variables based on the results of Section III. A simple procedure for generating Lognormal variables is given in [9]. The second part of the impulse response due to waves reflecting off of nearby scatterers is generated as in traditional SV models [14] except we use the statistics in Tables III–VI.

We can compare the simulated and measured channels using the distribution of the root mean square (rms) delay spread (τ_{rms}), and number of significant multipath components $(N_{10\ \mathrm{dB}})$. $N_{10\ \mathrm{dB}}$ is the number of components within 10 dB of the largest component. τ_{rms} is defined as the square root of the second central moment of a power delay profile [12].

The CDFs of τ_{rms} and $N_{10\ \mathrm{dB}}$ for measured and simulated channels are compared in Figs. 11 and 12. We extract the CDF for components diffracting near the body separately from components reflected from nearby scatterers. The delay spread of the reflections is larger than that of components diffracting around the body since the reflections are spread out over several clusters. Longer delay spreads are observed on the back of the body compared with the front. Despite simplifications of the APDP, the model matches the empirical data closely. Similarly, the reflected energy is spread out over more resolvable components than the energy diffracting near the body. The correlated Lognormal model accurately recreates the distribution of significant components near the body. The modified SV model

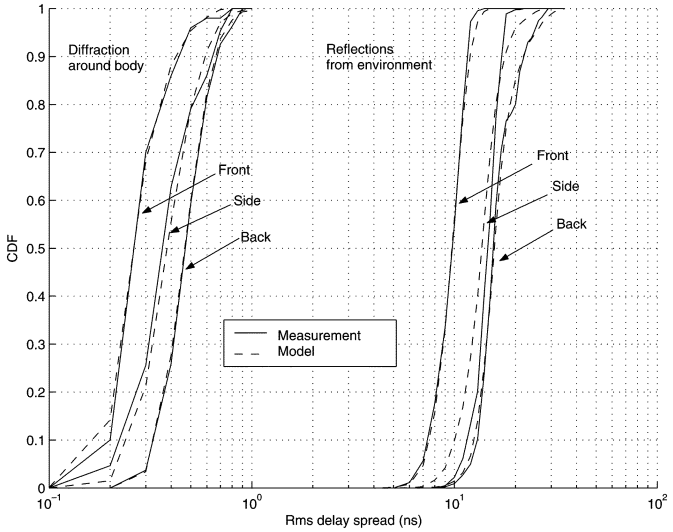

Fig. 11. Comparison of empirical and model RMS delay spread CDFs.

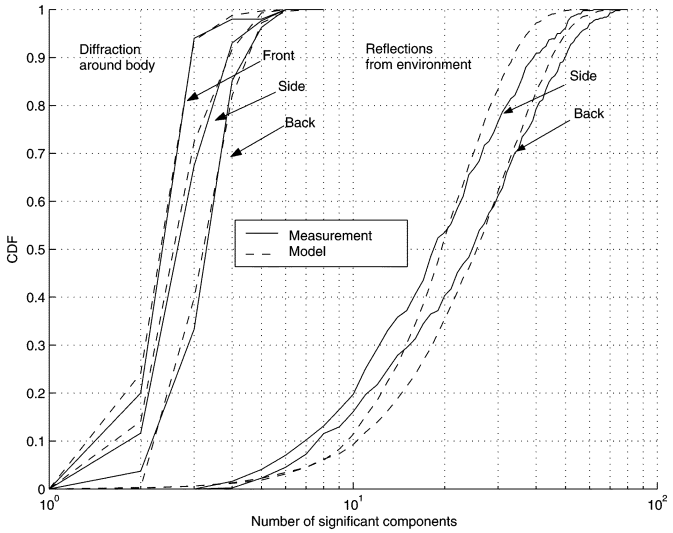

Fig. 12. Comparison of empirical and model significant component CDFs.

of the reflected components is accurate to approximately three components.

VII. Conclusion

We have proposed a procedure for measuring body area propagation in an indoor environment. Using this setup, we have shown that the body area channel consists of an initial cluster of components diffracting around the body, followed by subsequent clusters of components reflecting off of surrounding objects in the room. Due to the different propagation mechanisms, we propose modeling and measuring the local diffracting components and reflected components separately. Components diffracting around the body are well described by a high path loss exponent and correlated Lognormal variables. Subsequent clusters have a more complex structure that can be described by a modified S–V model. We have provided a small set of parameters to accurately characterize the complete channel based on our measurements and implemented the resulting model. Finally, we compared simulated and measured impulse responses and found a good match in terms of key communication metrics.

The values extracted in this campaign are specific to our particular antenna and office environment. However, the methodology can easily be reproduced and the model is general. We recommend further research on how different antennas, other environments or body positions, and the integration of UWB antennas into body worn devices will influence the parameters.

References

[1] IEEE 802.15.4a [Online]. Available: http://www.ieee802.org/15/pub/TG4a.html

[2] A. Fort, C. Desset, J. Ryckaert, P. DeDoncker, L. Van Biesen, and S. Donnay, "Ultra wide-band body area channel model," in *Proc. ICC*, Seoul, Korea, 2005, pp. 2840–2844.

[3] T. Zasowski, F. Althaus, M. Stager, A. Witttneben, and G. Troster, "UWB for noninvasive wireless body area networks: Channel measurements and results," in *Proc. IEEE Conf. Ultra Wideband Syst. Technol.*, Nov. 2003, pp. 285–289.

[4] A. Fort, C. Desset, J. Ryckaert, P. DeDoncker, L. Van Biesen, and P. Wambacq, "Characterization of the ultra wideband body area propagation channel," in *Proc. ICU*, Zurich, Switzerland, 2005, pp. 22–27.

[5] I. Kovacs, G. Pederson, P. Eggers, and K. Olesen, "Ultra wideband radio propagation in body area network scenarios," in *ISSSTA Proc.*, 2004, pp. 102–106.

[6] B. Gyselinckx, C. Van Hoof, J. Ryckaert, R. F. Yazicioglu, P. Fiorini, and V. Leonov, "Human++: Autonomous wireless sensors for body area networks," in *Proc. CICC*, 2005, pp. 12–19.

[7] A. Alomainy, Y. Hao, C. G. Parini, and P. S. Hall, "Comparison between two different antennas for UWB on-body propagation measurements," *IEEE Antennas Wireless Propag. Lett.*, vol. 4, pp. 31–34, 2005.

[8] B. Latre, G. Vermeeren, I. Moerman, L. Martens, F. Louagie, S. Donnay, and P. Demeester, "Networking and propagation issues in body area networks," in *Proc. SCVT*, 2004.

[9] A. F. Molisch *et al.*, "A comprehensive model for ultrawideband propagation channels," in *Proc. IEEE GLOBECOM*, vol. 6, Nov. 28–Dec. 2 2005, pp. 3648–3653.

[10] K. Siwiak, *Radiowave Propagation and Antennas for Personal Communications*. Boston, MA: Artech House, 1995.

[11] D. Cassioli, M. Z. Win, and A. F. Molisch, "The ultra-wide bandwidth indoor channel: From statistical model to simulations," *IEEE J. Sel. Areas Commun.*, vol. 20, no. 6, pp. 1247–1257, Aug. 2002.

[12] H. Hashemi, "The indoor radio propagation channel," *Proc. IEEE*, vol. 81, no. 7, pp. 943–968, Jul. 1993.

[13] K. P. Burnham and D. R. Anderson, *Model Selection and Multimodel Inference: A Practical Information-Theoretic Approach*, 2nd ed. New York: Springer-Verlag, 2002.

[14] A. Saleh and R. A. Valenzuela, "A statistical model for indoor multipath propagation," *IEEE J. Sel. Areas Commun.*, vol. 5, no. 2, pp. 128–137, Feb. 1987.

Andrew Fort (S'04), photograph and biography not available at the time of publication.

Julien Ryckaert, photograph and biography not available at the time of publication.

Claude Desset (S'94–M'01), photograph and biography not available at the time of publication.

Philippe De Doncker, photograph and biography not available at the time of publication.

Piet Wambacq (S'89–M'91), photograph and biography not available at the time of publication.

Leo Van Biesen (M'90), photograph and biography not available at the time of publication.